

# Thermomechanical failure analysis of IFMIF-DONES target under off-nominal extreme conditions

M.A. Vázquez-Barroso <sup>a</sup>,\*, C. Torregrosa-Martín <sup>b</sup>, J. Maestre <sup>b</sup>

<sup>a</sup> University of Granada, UGR-DONES, CITAI Ciudad Industrial, Avenida de Incar 31, Escúzar, Granada, 18130, Spain

<sup>b</sup> IFMIF-DONES España, UGR-DONES, CITAI Ciudad Industrial, Avenida de Incar 31, Escúzar, Granada, 18130, Spain

## ARTICLE INFO

### Keywords:

DONES  
EUROFER  
Lithium  
Phase-change  
Fusion technology  
Mechanical failure

## ABSTRACT

IFMIF-DONES will be a radiological facility for material irradiation replicating conditions expected in future fusion reactors. It will employ a 40 MeV deuteron beam directed at a liquid Li target circulating at 15 m/s to generate high-energy neutrons, depositing 5 MW. The Back-Plate (BP), placed immediately downstream of the Li, separates the vacuum of the accelerator and target chambers from the low-pressure He atmosphere housing the irradiation modules. A critical scenario postulates an eventual loss of liquid Li curtain thickness without shutting down the beam, risking a direct or partial deuteron beam impact on the BP causing large power deposition. This study provides the BP dynamic thermomechanical response, aiming at characterizing the involved timings in the impact-triggered events, such as mechanical failure, melting or vaporization. This is important to evaluate the eventual mobilization of the BP volatilized activated material and the available timings for beam shutdown. The methodology involves Monte-Carlo simulations for power deposition data integrated into a Finite Element model in ANSYS for transient thermal and structural analyses. Results include timings for melting, vaporization, and mechanical response as function of the beam footprint area and the Li jet thickness reduction.

## 1. Introduction and objectives

Since the early 1990s, the fusion materials scientific community has been advocating for the development of a neutron source for the qualification of materials to be used in future fusion power reactors, such as the DEMONstration power plant (DEMO) described in Refs. [1,2]. The research was designed to be conducted in an irradiation facility where material samples would be subjected to fusion-like radiation conditions, as highlighted in the Refs. [3,4].

The International Fusion Materials Irradiation Facility-DEMO Oriented Neutron Source (IFMIF-DONES), detailed in Ref. [2], represents an initial step aimed at providing relevant data for the early engineering design of DEMO, as outlined in Refs. [4,5]. The facility will operate a 5 MW continuous wave deuteron linear accelerator, which will produce neutrons via the deuteron-lithium target interaction. The aim is to reach a maximum dose of 20 dpa in a full power year in the material specimens within the initial operation phase.

As a radiological facility, the IFMIF-DONES design must ensure the safety of the public, its personnel and the environment according to the Spanish regulations (Refs. [6–8]). In accordance with the aforementioned criteria, a detailed account of the IFMIF-DONES safety

approach was presented in Refs. [9,10], which was developed following the defense-in-depth principles, identifying reference accident scenarios, and outlining the protective measures established following a prevention-detection-mitigation framework.

The Lithium Systems of the IFMIF-DONES facility are responsible for providing a stable liquid lithium jet with a controlled thickness of 25 mm. A neutron flux with a fusion-like energy spectrum would be generated via the impact of a 125 mA current and 40 MeV D<sup>+</sup> beam into the Li jet, which absorbs and removes a total deposited power of 5 MW. As depicted in Ref. [11], this interaction would take place in vacuum condition on a rectangular footprint area ranging from 10 × 5 to 20 × 5 cm<sup>2</sup>. The generated neutrons pass through the Back-Plate (BP) to reach the samples. The BP, represented in Fig. 1 as shown in Ref. [12], closes the Target Vacuum Chamber (TVC) and separates its inner vacuum from the Test Cell (TC) atmosphere filled with Helium at a pressure between 2 and 9 kPa. In the footprint region, the width of the BP in the beam direction ranges from 1.8 to 3 mm. Its design is intended to achieve the optimal curvature, facilitating the greatest possible flux of neutrons through the structure. Concurrently, it serves to maintain the Li jet in a liquid state within the vacuum conditions of the TVC.

\* Corresponding author.

E-mail addresses: [manvazbar@ugr.es](mailto:manvazbar@ugr.es) (M.A. Vázquez-Barroso), [claudio.torregrosa@ifmif-dones.es](mailto:claudio.torregrosa@ifmif-dones.es) (C. Torregrosa-Martín), [jorge.maestre@ifmif-dones.es](mailto:jorge.maestre@ifmif-dones.es) (J. Maestre).

<https://doi.org/10.1016/j.fusengdes.2025.115068>

Received 16 January 2025; Received in revised form 20 March 2025; Accepted 8 April 2025

Available online 25 April 2025

0920-3796/© 2025 The Authors. Published by Elsevier B.V. This is an open access article under the CC BY license (<http://creativecommons.org/licenses/by/4.0/>).

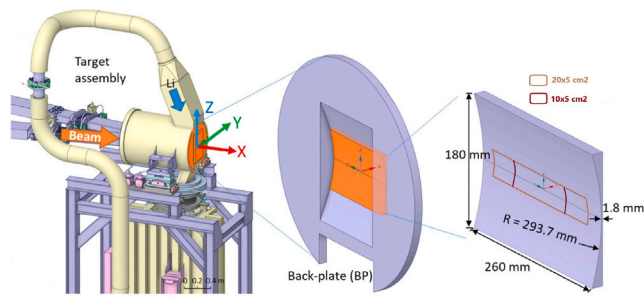


Fig. 1. BP geometry.

One potential risk of the operation is the eventual loss of the liquid Li jet thickness without sufficient time to shutdown the beam, which would imply the direct or partial impact of the D+ beam on the BP with the consequent large power deposition beyond its acceptance limits. This event, which can occur with an instability of the curtain thickness within only 4–5 mm, would induce a rapid power deposition in the BP behind the Li, triggering a dynamic response characterized by a sudden temperature increase, thermal deformations, stresses, and its eventual failure.

A detailed characterization of the BP response to partial or direct beam impingement and the subsequent chain of events is necessary as part of this accident analysis. The BP failure could trigger the mobilization of part of the activated inventory in the BP upstream the accelerator vacuum chambers due to the sudden helium entrance from the TC as a consequence of the vacuum loss. This event may be reduced or mitigated with the actuation of dedicated safety systems to shutdown the beam and isolate the potentially damaged target from the rest of the accelerator to contain the eventual mobilization of activated inventory.

A comprehensive understanding of the failure modes (mechanical, melting and vaporization) of the BP and the associated timings is crucial for the definition of requirements for such detection and mitigation safety systems. The results of this characterization are important both in terms of defining the detection and actuation time requirements, as well as their required reliability (which is based on the potential consequences of not mitigating the accident).

Finite elements simulations are commonly carried out in accelerator facilities to estimate the thermo-mechanical response of components due to beam-matter interaction, as those reported in Refs. [13–16]. In general, these simulations are used to identify steady-state temperatures, stresses and cooling, as well as transient responses for target applications or abnormal operation. In comparison with these studies, the simulations reported in this article deal with a much higher power density caused by the short range of the 40 MeV deuterons (up to 2 MW/cm<sup>3</sup> at the maximum deposition depth), as well as an eventual continuous power deposition until the beam is shutdown.

## 2. Methodology

The modeling process for the BP failure sequence have comprised a number of steps. The first of them is the estimation of beam energy deposition in the BP for different Li curtain thickness reduction and beam footprint size. This is done by the SRIM software (described below). Different Li curtain thickness reductions in the range from 5 up to 25 mm are considered to study the variation of the energy deposition profile in the BP.

The second step involves the introduction of the beam energy deposition profiles obtained by SRIM as an internal heat load into an ANSYS Finite Elements (FE) model for simulating the BP thermo-mechanical response. This importation is done by post-processing the SRIM results using a MATLAB script. The importation is one-way coupling, i.e. changes of density in the BP due to the temperature increase are

not taken into account in the computed energy deposition by SRIM. In addition, the ANSYS FE simulations use temperature-dependent properties of EUROFER97, which have been introduced by extrapolation of available experimental data to high-temperature ranges based on the properties of other ferritic-martensitic steels (described below).

Once the ANSYS FE models are set, thermal-transient simulations are performed to predict the timings in which the BP material would reach the onset of melting and vaporization. Finally, structural-transient simulations are also performed in ANSYS transferring the thermal results with the intent to estimate the timings for potential mechanical failure of the BP based on stress and deformation.

## 3. Computational models

### 3.1. Modeling beam-matter interaction to obtain the power deposition in the BP

The interaction of high-energy particle beams with solids results in the energy deposition within the material, which in turn causes a sudden non-uniform temperature increase. In the present study, calculations of energy deposition by the D+ beam, which presents a quasi-uniform rectangular profile in all the footprint region ranging from 10 to 20 × 5 cm<sup>2</sup>, in the BP material after passing through a liquid Li curtain of reduced thickness are conducted using the SRIM Software (Stopping Range of Ions in Matter), which employs Monte-Carlo simulations under a quantum mechanical treatment of ion-atom collisions, as detailed in Ref. [17].

Li curtain thickness in normal operation is expected to be 25 mm. We evaluate the effect of Li curtain thickness reduction by performing a parametric analysis considering thickness reductions ranging from 5 up to 25 mm (no Li at all) with steps of 2 mm leading to a total of 11 scenarios for each beam size configuration. Each scenario results in a different power deposition profile in the BP. The peak of power deposition along the beam direction occurs when incident particles decelerate, depositing the remaining energy in the vicinity of the so-called Bragg-peak. The incident energy, which is different for each Li thickness reduction, influences the Bragg-peak penetration depth within the BP material.

As previously mentioned, the simulations are based on one-way coupling. For this reason, the corresponding density change in the BP due to its rapid temperature increase that would influence the beam-matter interaction are not taken into account (the so-called hydrodynamic tunneling effect). This effect involves a Bragg-peak displacement towards a deeper penetration of the beam in the material. We evaluated the errors induced by this one-way coupling by analyzing the maximum Bragg-peak displacement that could take place in the BP due to density variations from 300 °C to its vaporization point. This evaluation indicates a maximum discrepancy in the Bragg-peak penetration of only 0.54 mm when assuming the density at the vaporization point. This effect is deemed to be encompassed by the different scenarios involving the reduction in thickness of the Li curtain and is considered a second-order influence over the final result. Therefore, we consider that is not required to perform a two-way coupled simulation (as performed in the Ref. [18]).

### 3.2. Finite elements model of the back-plate

The BP geometry is reduced to a two-dimensional model in ANSYS, situated in the vertical symmetry plane. It is postulated that the thermal and mechanical effects will be more pronounced in the beam direction, where larger temperature gradients are anticipated in comparison with other directions. Furthermore, the center of the BP footprint region is deemed far enough from the limits of the irradiated volume to neglect local temperature variations in the transverse direction, conforming the adiabatic condition and justifying the reduction to a two-dimensional

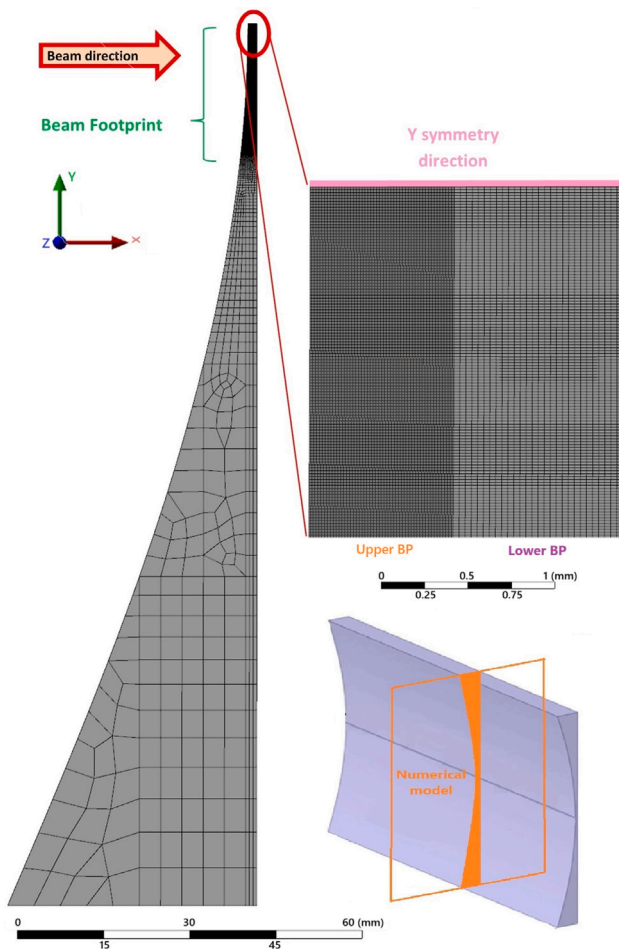


Fig. 2. BP numerical model and meshing for the 13 mm Li thickness reduction scenario and  $20 \times 5 \text{ cm}^2$  beam size configuration.

model. Additionally, a symmetry plane is introduced accounting with the existing parallelism in the BP curvature.

A model with different meshing for each Li curtain reduction scenario is developed with the intention of tailoring the power density input derived previously in Section 3.1. The number of divisions along the beam direction in the irradiated part of the footprint is fixed at one hundred in order to match with the maximum SRIM accuracy, thereby maintaining the Bragg-peak power deposition values. It is noteworthy that meshing size is designed accounting with the characteristic diffusive length (see Section 3.4), indicating that thermal effects will be accurately captured without being influenced by numerical diffusion or spatial discretization errors. Fig. 2 depicts the BP model, including the meshing for the 13 mm Li thickness reduction scenario and  $20 \times 5 \text{ cm}^2$  beam size configuration.

### 3.3. Modeling EUROFER97 properties

EUROFER97 is one of the proposed materials for fusion reactors that has been identified for further investigation within the context of IFMIF-DONES and it has been selected as the BP structural material expecting to resist irradiation campaigns in the absence of better proposals.

To perform our analysis, available data of EUROFER97 (extracted from Refs. [19–22]) have been employed, supplemented by extrapolations to higher temperatures from analogous low-carbon ferritic-martensitic steels and from other similar stainless steels (derived from Refs. [23–27]). The list of temperature-dependent properties included

in our computational models, along with the references from where they are extrapolated depending on the temperature range, are detailed in Table 1.

The behavior of EUROFER97 under thermo-elasto-plastic deformations is included. It has been well documented in the literature that it is susceptible to radiation-induced brittleness (described in Ref. [28,29]) and defect formation. However, our analysis does not consider the influence of radiation hardening and high strain rates due to the anticipated significant softening effects at elevated temperatures (detailed in Refs. [30–32]).

Thermal properties have been extrapolated from the experimental data following the slopes obtained from the references at high temperatures for other steels. In order to set the plastic response of the material, a multilinear isotropic hardening model is considered, which results specially suitable for large strain, proportional loading situations (when the orientation of the principal stresses does not change during the course of loading). It is necessary to have the knowledge of both the true plastic strains and the corresponding true stress values across a range of temperatures, in addition to information about structural parameters as Young modulus or Poisson ratio. All the considered curves, experimental (continuous) and calculated from extrapolated data (dashed) are shown in Fig. 3.

Once the mechanical properties in terms of stress–strain response have been defined, it is necessary to establish a criterion for determining when the BP might fail. In this sense, failure is defined as the point at which the BP loses its integrity, either as a result of the changes in properties induced by the increase in temperature (thermal failure) or by the plastic deformations (mechanical failure), leading to the entrance of helium from the TC atmosphere into the TVC. Therefore, the timing of the potential failure of the BP must be inferred by analyzing the post-simulation thermal-structural results to determine when a defined failure criterion is reached.

Initially, the strain-to-rupture of EUROFER97 was considered as a potential mechanical failure criterion by definition of this property (last deformation value before fracture in tensile tests). Stress results quite sensible to rapid deformations and thermal loads, thus becoming not reliable for failure criterion in this context. In the literature, it ranges from 21.5% reported in Ref. [26] to 38.7% given in Ref. [19] at  $700 \text{ }^\circ\text{C}$ . The presence of elevated temperatures exceeding a thousand  $^\circ\text{C}$ , at which the BP material becomes highly ductile make it challenging to establish a common threshold for structural failure in the footprint volume. Nevertheless, we establish as a mechanical failure criterion for a plastic fracture when a 30% strain is reached in a sufficient portion of the BP width (approximately 50% in the central region of the footprint). Note that our model is not designed for giving results after fracture, instead we try to infer when it might happen based on the total strain.

Concurrently, the progressive heating process of the BP results in a loss of consistency due to the change of state of the bulk inventory from a solid to a liquid and/or gas. This phenomenon, in conjunction with the existing pressure difference between the TC helium atmosphere and the inner TVC vacuum, is regarded as a potential failure mode. Consequently, it is conservatively postulated that a thermal failure criterion may be established when 75% of the material in the BP width at the center of the footprint region has melted. It is clear that a 100% of material thickness melted will lead to the He entrance from the TC atmosphere, but at some point the remaining solid part will fail as a consequence of the progressive loss of consistency, the external pressure gradient and the stress concentration in a reduced thickness portion. In addition, the temperature of the remaining portion may be underestimated as a consequence of not including the tunneling effect in the power density profile. For this reason, it was considered that a solid portion of less than half millimeter thickness at high temperatures, which corresponds to a 25% of the BP thickness in the centerline in the beam direction when the rest have melted, will be enough for triggering this situation.

**Table 1**  
List of EUROFER97 temperature dependent properties included in the model.

Property	References	
	Experimental	Extrapolation
Density	300–700 °C [19]	>700 °C [23]
Melting/boiling temperature	1506.85/2826.85 °C [23]	
Isotropic thermal conductivity	300–600 °C [19,20]	>600 °C [23]
Enthalpy	300–600 °C [19,20]	>600 °C [23,24]
Isotropic instantaneous coefficient of thermal expansion	300–500 °C [19]	>500 °C [23]
Isotropic elasticity: Young modulus, Poisson ratio	300–700 °C [19,21]	>700 °C [25]
Multilinear isotropic hardening: plastic stress–strain	300–700 °C [19,21,22]	>700 °C [26,27]

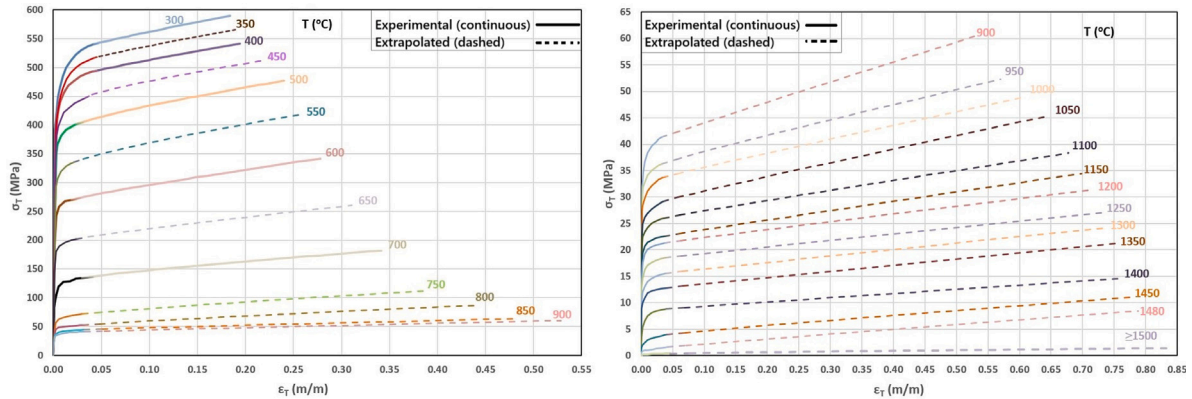


**Fig. 3.** True stress–strain curves for EUROFER97.

### 3.4. Transient-thermal model

Transient-thermal simulations yield spatial temperature distributions over time. They are used to estimate critical events associated with melting and evaporation phenomena and to provide the response of the modeled structure to heat loads. The corresponding input for each Li curtain thickness reduction and beam size configuration scenario is effectuated through the application of the power density distribution calculated following the steps in Section 3.1.

Mesh elements type PLANE292, which corresponds to a linear representation, are implemented in the model, along with implicit integration with variable time discretization scheme. It is expected that these elements type help to provide stability when extreme temperature gradients appear. Furthermore, linear distribution of heat strain is expected for the forthcoming structural simulations.

In order to ensure the accuracy of the results attached to the selected mesh defined in Section 3.2, the characteristic diffusive length  $L$  is calculated for linear heat transfer, as reported in the Ref. [14], as two times the square root of the thermal diffusivity  $\alpha$  multiplied by the characteristic timescale  $\tau$  (milliseconds in our case):  $L = 2\sqrt{\alpha \cdot \tau}$ . Note that diffusivity is taken as the maximum value reported in the literature for the considered temperature range, matching with the normal operation temperature of 300 °C (7.05 mm<sup>2</sup>/s determined in Ref. [20]). This result in a characteristic diffusive length of 0.17 mm.

In line with the adiabatic condition, it is considered that other heat transfer mechanisms from conduction, such as radiation to the environment or convection, are second-order effects in solid metals for the predicted timescales of milliseconds, and therefore they are not included. Phase-change effect is reflected in the description of thermal properties such as enthalpy and density in the vicinity of these temperatures (for both melting and vaporization).

It is considered that an envelope estimation for thermal failure timing will be when 75% of the width in the central region of the footprint passed the melting temperature, as described in Section 3.3. In addition, the amount of mobilizable inventory can be estimated as the volume above the melting point at that time. The timing of the onset of melting and vaporization and the temporal evolution of the melted

fractions (25% and 75% of the BP material thickness) are determined as they provide insight into the heating rate of the BP material within the beam footprint region.

### 3.5. Transient-structural model

Transient structural analysis calculates the response to temporary loads, taking into account the full temperature–time profile estimated in the previous thermal-transient simulations, until the BP material loses too much consistency. The purpose is to elucidate the time required to reach the mechanical failure criteria discussed in Section 3.3. Mesh elements type PLANE183 (quadratic order) are implemented in the model, along with implicit integration with variable time discretization scheme.

To improve the accuracy of the results in the two-dimensional model, a plane (constant) strain condition is assumed along the transverse direction to the beam, as discussed in Section 3.2. A pressure load of 9 kPa is applied to the external part of the BP facing the TVC, as well as the pertinent impositions to prevent rigid body motion.

In a first instance, the mechanical model accounts the material transition to the liquid phase via the definition of the structural properties, which maintain the last value reported in the solid state for increasing temperatures. This assumption implies that some degree of structural consistency is given to the liquid phase, but as a consequence it is possible to extend structural results in the remaining solid part even after melting effect occurs in the material. Nevertheless, results must be carefully interpreted, paying special attention to the portion supposed to be in liquid phase as the attached results to these areas should not be included. In addition, there are inertial effects from the melted part with structural consistency that may provoke an overestimation of the deformation results, as it keeps attached to the structure during the simulation time.

To remove those inertial effects, a second model is proposed to understand the behavior of the solid part of the structure by removing the elements above the melting point at a fixed time, with the mesh remaining unaltered in the remainder of the beam footprint region. This model is developed once the results of the transient thermal simulation

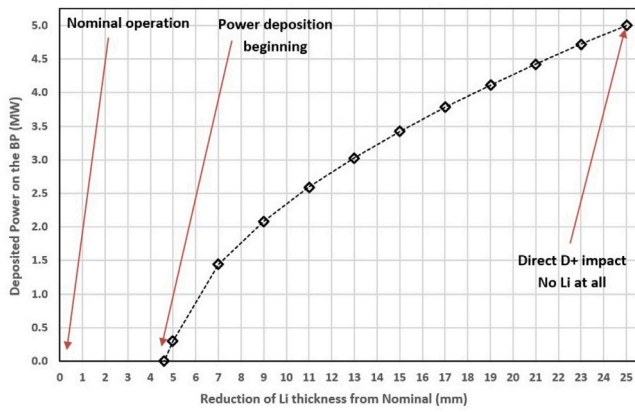


Fig. 4. Total power deposited in the BP.

Table 2

Depth of the Bragg-peak, irradiated zone width and characteristic length for thermal diffusion for the different Li jet thickness reduction model meshing.

Thickness reduction (mm)	Bragg-peak depth (mm)	Irradiated BP thickness (mm)	Min. time step ( $\mu$ s)
25 (no Li)	1.76	1.87	11.5
23	1.59	1.71	10.4
21	1.43	1.52	8.2
19	1.26	1.35	6.5
17	1.09	1.18	4.9
15	0.90	1.00	3.5
13	0.74	0.83	2.4
11	0.56	0.65	1.50
9	0.38	0.46	0.75
7	0.20	0.28	0.28
5	2.7E-3	0.09	2.9E-2

for the entire model have been estimated. For this reason, it is presented with the simulation results in Section 4.4.

#### 4. Simulation results

##### 4.1. Power deposition in the BP and heat load input in ANSYS

A MATLAB script was employed to collect the deposited power density in the BP for each of the Li curtain thickness reduction scenarios. The power deposition distributions across the BP thickness for both beam configurations are identical, differing only in power density values: the focused beam mode of  $10 \times 5 \text{ cm}^2$  results in double the power density respect to the  $20 \times 5 \text{ cm}^2$  one, applied in half of the volume, which results in the same total power deposited of 5 MW.

Fig. 4 illustrates the total power deposition in the BP material. It is noteworthy that below a reduction in Li curtain thickness of 4.6 mm, the D+ beam does not significantly deposit power in the BP material, as the Bragg-peak remains within the Li curtain. The power deposition increases logarithmically with reduction in Li curtain thickness, reaching a point of near complete stopping of the beam inside the BP in the direct beam impact scenario.

In addition, Table 2 presents the depth of the Bragg-peak at the upper part of the footprint region together with the associated thickness of the irradiated volume.

It is important to note that the number of divisions in the beam direction at the upper region of the footprint is fixed at one hundred, thereby ensuring that the condition of smaller cell sizes in comparison with the characteristic diffusive length (0.17 mm) is effectively met. It is also interesting to apply the characteristic diffusive length definition (see Section 3.4) in order to estimate the minimum time step required to capture thermal effects in the irradiated volume of the BP at each iteration.

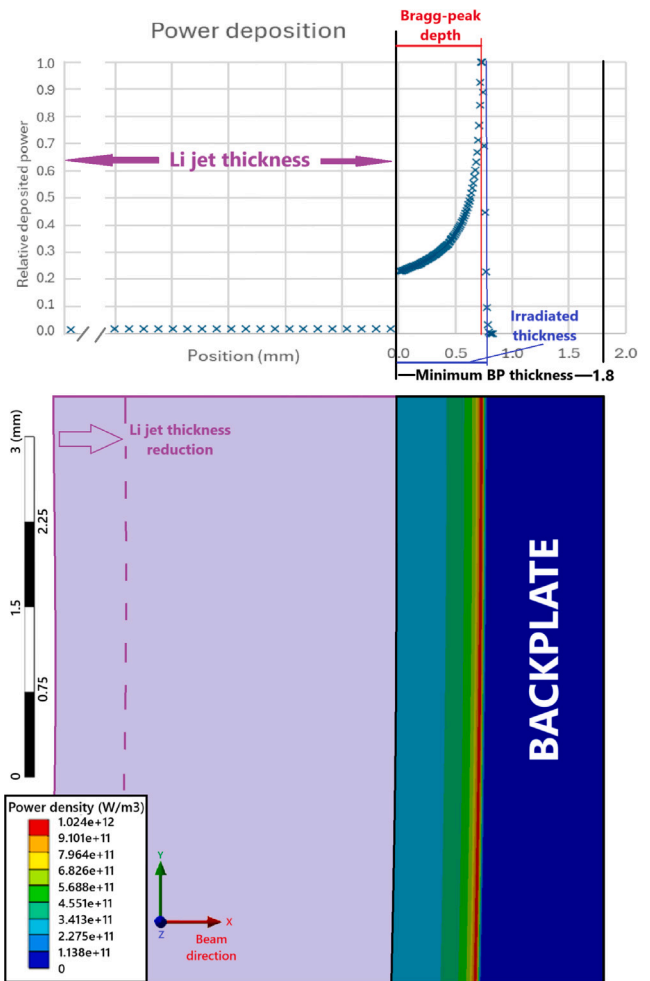


Fig. 5. Power density input heat load for a 13 mm Li thickness reduction scenario with  $20 \times 5 \text{ cm}^2$  beam size configuration.

The power density distributions are imported to ANSYS through the elaboration of a table in MATLAB indicating spatial coordinates for each of the one hundred values calculated with SRIM. Fig. 5 presents how the input power density in ANSYS is implemented for the specific scenario of 13 mm Li jet thickness reduction in  $20 \times 5 \text{ cm}^2$  beam size configuration.

##### 4.2. Timing for thermal related events

Thermal-transient simulations determine the evolution of the temperature profile in the BP material, focusing on the beam footprint region. Fig. 6 presents examples of temperature distribution contour plots at specific times for the 13 mm Li thickness reduction scenario with a  $20 \times 5 \text{ cm}^2$  beam size configuration.

The timescales for the onset of melting and vaporization were derived from the maximum temperature profiles determined by the thermal simulations. Additionally, the times required to melt 25% and 75% of the material along the BP thickness at the beam footprint region were extracted. A summary of these results is provided in Table 3. In addition, they are illustrated in Fig. 7.

A comparative analysis of the two beam size configurations indicates that the onset of melting and vaporization occurs approximately twice as fast in the focused mode compared with the  $20 \times 5 \text{ cm}^2$  configuration. It is observed that times required to reach melting onset are similar independently of the Li jet thickness reduction. Something

**Table 3**  
Timings for thermal related events for different Lithium curtain thickness reductions and beam configurations.

Li jet thickness reduction (mm)	$t_{\text{onset melting}}$ (ms)		$t_{25\% \text{ melted}}$ (ms)		$t_{75\% \text{ melted}}$ (ms)		$t_{\text{onset vap}}$ (ms)	
	$20 \times 5$	$10 \times 5$	$20 \times 5$	$10 \times 5$	$20 \times 5$	$10 \times 5$	$20 \times 5$	$10 \times 5$
25 (no Li)	12.5	5.55	20.0	10.2	35.3	18.4	43.3	14.3
23	17.8	8.26	21.5	10.7	33.8	17.5	88.0	43.3
21	20.6	8.78	23.6	11.3	33.2	17.5	104.0	51.6
19	21.2	8.85	24.3	11.4	33.2	17.4	119.0	56.6
17	21.2	8.85	24.3	11.4	46.0	27.5	131.0	58.8
15	21.2	8.85	24.1	11.4	63.0	42.9	137.2	59.3
13	21.0	9.01	23.6	11.3	86.4	69.6	141.3	60.2
11	20.6	8.77	22.4	10.8	114.5	108.0	140.9	55.0
9	19.8	8.59	31.1	14.4	148.0	121.0	140.7	58.8
7	20.9	8.05	51.1	27.2	191.8	150.1	143.8	59.1

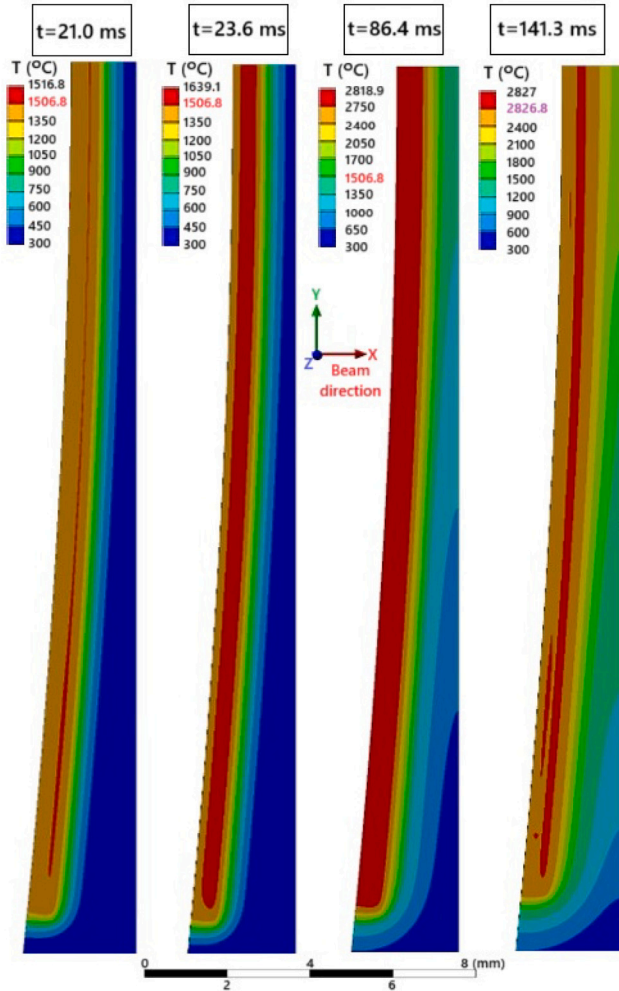


**Fig. 6.** Temperature distribution at specific times for the 13 mm Li thickness reduction scenario with  $20 \times 5 \text{ cm}^2$  beam size configuration.

similar applies to vaporization onset up to 17–19 mm of Li jet reduction, when it tend to accelerate. This effect is associated with heat conduction, which is impeded as the non-irradiated volume diminishes (i.e., when Li jet reduction increases). The reduction in heat conduction through the material results in a faster onset of melting/vaporization.

Furthermore, in both beam size configurations the time required to melt the 25% of the BP central axis thickness material stabilizes above 11 mm of Li thickness reduction, whereas for the 75% melting it occurs after only 19 mm reduction. It is once more evident that the process of heat conduction delays the occurrence of these thresholds.

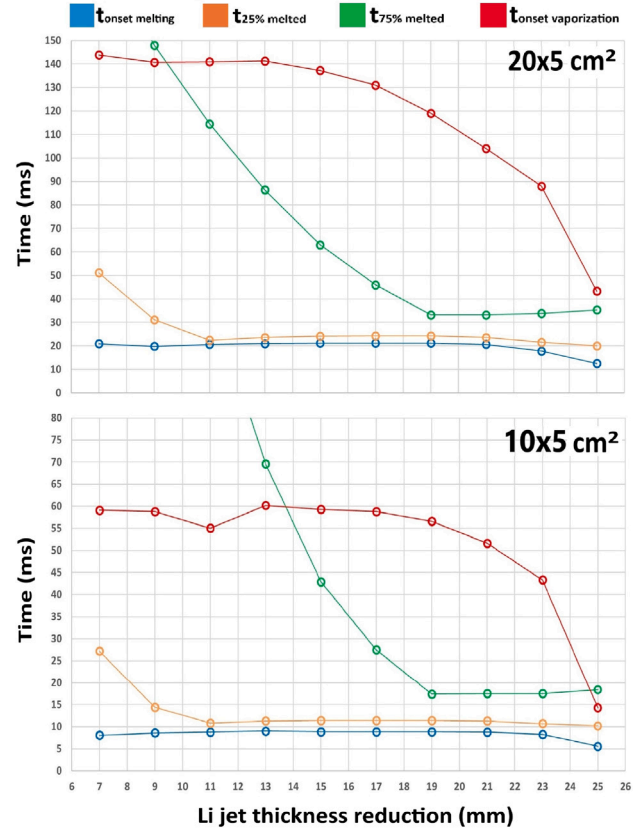


**Fig. 7.** Timings related with melting and vaporization onsets and with 25% and 75% of width melting for both beam operation modes.

The assumption of a constant reduction in the Li curtain thickness is useful for determining the heat load and for visualizing the BP response to this specific energy spectrum. In reality, the Li curtain thickness reduction will vary exponentially over time and, consequently, the timescales presented in Fig. 8 encompass an envelop of the reduction process for each of the beam size configurations.

#### 4.3. Timing for mechanical failure

Transient-structural analysis of the BP provide profiles of total deformation and strain within the BP material thickness as response to the thermal load calculated in the thermal-transient simulations, with a particular focus on the beam footprint region. The timescale for mechanical failure is assessed by determining strain, paying also special attention to the associated deformation profile.

Figs. 9 and 10 illustrate the total strain and deformation, respectively, of the BP for the 13 mm Li thickness reduction scenario with  $20 \times 5 \text{ cm}^2$  beam size configuration at specific times.

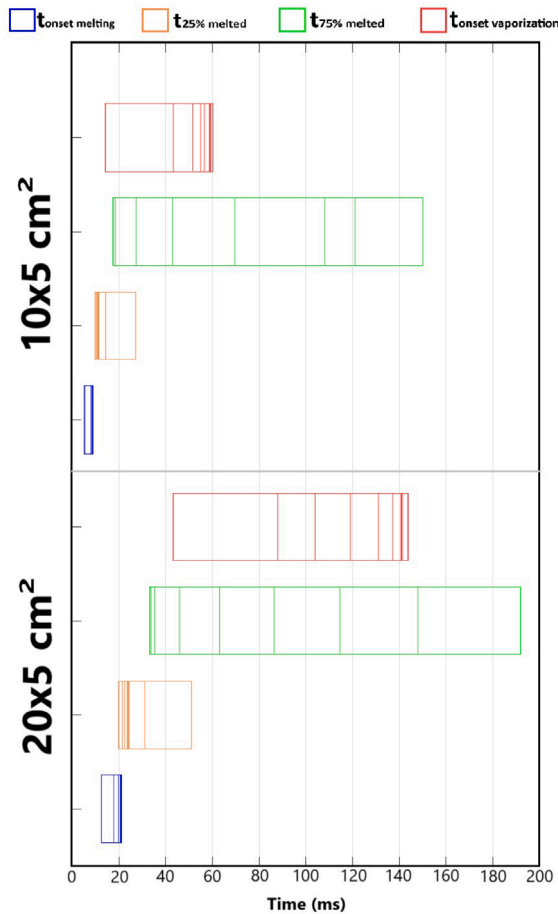


Fig. 8. Enveloping timings related with thermal results for both beam mode configurations.

Total deformation plot indicates a significant tendency to deform downstream in the beam direction, which is in opposition to the helium pressure applied from the TC atmosphere. The maximum displacement from the nominal position is observed at the center of the beam-impinged area, exceeding 6 mm in the final converged time step. Given the initial 2 mm separation between the BP and the module housing the samples, deformations beyond this value suggest a contact phenomenon between these systems in addition to the corresponding heating of the samples module, which will be addressed in future analyses, especially in relation to metal vapor source terms.

Strain distribution indicates that the highest strain values correspond to the BP section in proximity to the symmetry axis at the Bragg-peak, where melting onset is firstly reached. As discussed in 3.3, the BP material becomes more ductile with increasing temperature, allowing higher strain values without fracturing. Nevertheless, the numeric model considers that the melted material is perfectly plastic with negligible yield strength. In the solid parts, strain does not exceed 20%. Therefore, these simulations do not clearly indicate when the mechanical failure criteria is reached and thus the timing for this event.

Additionally, a strain concentration is observed in the BP material thickness within the beam footprint region farthest from the symmetry axis. This is probably due to the extreme temperature gradient with the non-irradiated volume provoking fast properties degradation, and to the apparition of a pivot joint where high moments are observed. In addition, it corresponds to a region where the temperature profile is over or near the melting onset, and thus structural effects become meaningless in the liquid phase.

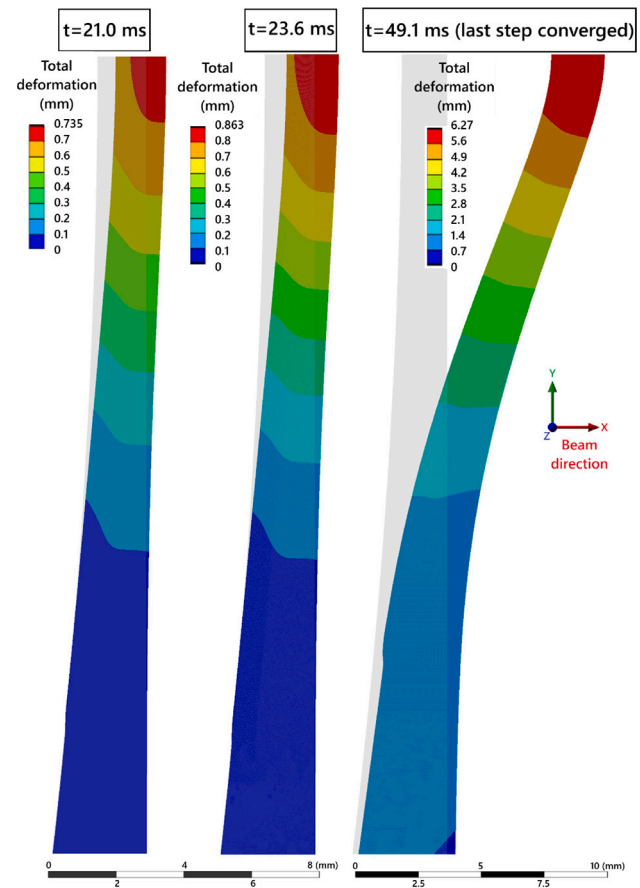


Fig. 9. Total deformation of the BP at specific times for the 13 mm Li thickness reduction scenario with  $20 \times 5 \text{ cm}^2$  beam size configuration.

#### 4.4. Reduced thickness model (melted material removal)

We conducted an analysis of a reduced-thickness sample in which the material exposed to temperatures above the melting onset at a fixed time was removed. The portion to be removed is determined based on the results of the thermal transient analysis.

Fig. 11 illustrates the 50% reduced-thickness models for 13 mm of Li thickness reduction in the  $20 \times 5 \text{ cm}^2$  beam size configuration, and Fig. 12 presents the 75% reduction model for a 23 mm reduction of Li curtain thickness scenario in the  $20 \times 5 \text{ cm}^2$  beam size configuration.

The structural results (deformation and strain distributions) for the aforementioned scenarios are presented in Fig. 13 for the 13 mm Li thickness reduction scenario and 50% reduction, and Fig. 14 for the 23 mm one with 75% reduction, both for the  $20 \times 5 \text{ cm}^2$  beam mode configuration.

Fig. 13 shows that the maximum deformation is nearly identical in the reduced-thickness model and in the complete one, with maximum strain concentrated at the interface between the removed volume and the rest of the BP material. This is probably due to the exclusion of dynamic and inertial effects in the reduced-thickness model, derived from the incorporation of material in the liquid phase with structural consistency in the complete one. In addition, both exhibit deformation in the beam direction against the pressure, probably caused by thermal expansion effect (reinforced in the complete scenario by the numerical expansion of the melted material).

Concerning the scenario considering a 75% of thickness reduction shown in Fig. 14, something similar to the previous case is observed, with similar deformation and strain distributions and discrepancies justified by inertial and dynamic effects attached to the melted material in the complete model.

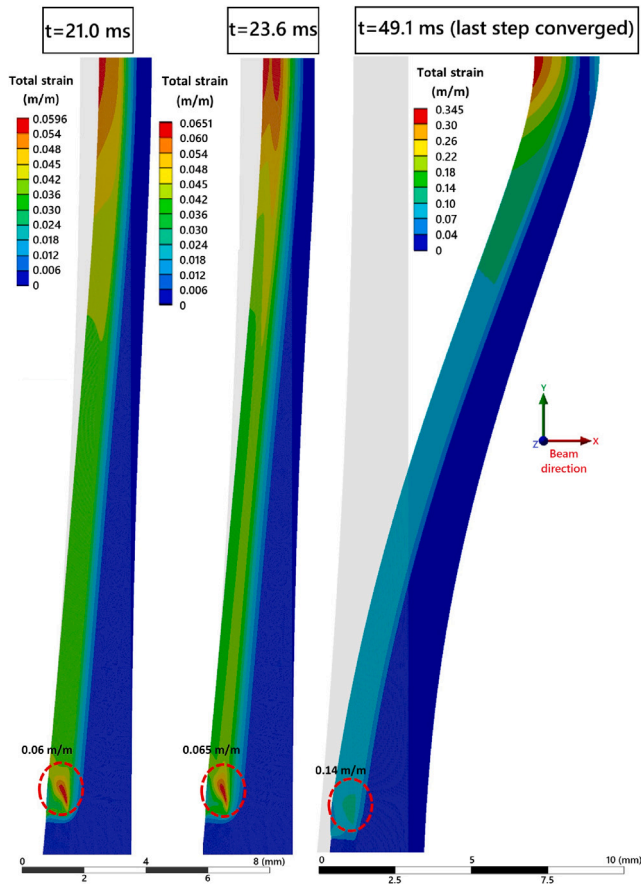


Fig. 10. Total strain of the BP at specific times for the 13 mm Li thickness reduction scenario with  $20 \times 5 \text{ cm}^2$  beam size configuration.

In conclusion, we can derive that an intermediate result between the two presented scenarios will occur in reality, as inertial and dynamic effects in fact may have some influence over the final distributions but in a lesser extent compared with the case of no material over the melting point.

5. Conclusions

The energy deposition of the incident 40 MeV D+ beam inside the BP material (EUROFER97) has been calculated for the presented scenarios using SRIM and MATLAB. A series of thermo-mechanical simulations has been conducted in ANSYS, in which the thickness reduction and the impinged area (beam size configurations) of the Li curtain were varied. In the case of  $20 \times 5 \text{ cm}^2$  configuration, the melting onset occurs between 12 and 21 ms, and vaporization one in a range from 43 to 144 ms, while for the 75% of melted material, it is observed in 33 to 192 ms. For the  $10 \times 5 \text{ cm}^2$  configuration, temperatures in the melting onset are obtained between 5 and 9 ms, in vaporization from 14 to 60 ms and 75% melting in 17 to 150 ms.

The vaporization onset time is of great importance in terms of safety, as it indicates the time before the BP material begins to mobilize in gaseous form. In addition, the time required to melt the 75% of the BP material thickness at the beam footprint region is considered as the indicator for thermal failure. It results interesting to compare both tendencies to identify the amount of mobilizable material when thermal failure occurs or, conversely, time to start to appear this mobilizable material in gaseous form after thermal failure occurs (if the beam continues impinging the footprint region of the BP). The 75% melted curve falls below the vaporization curve for specific Li thickness

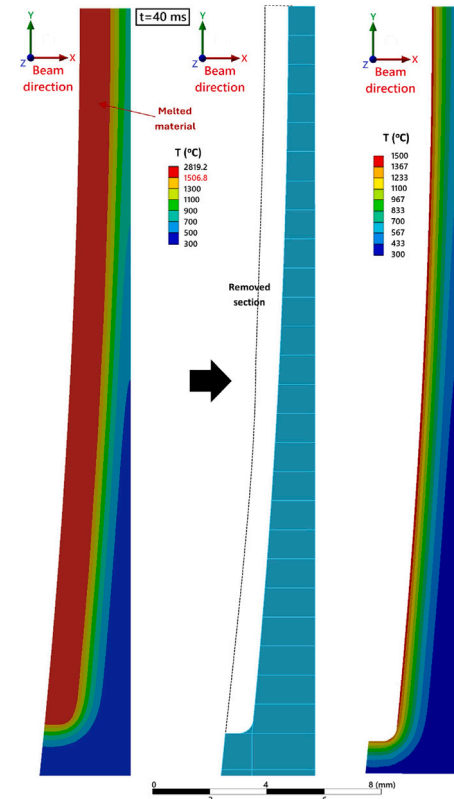


Fig. 11. Reduced model for the 13 mm Li thickness reduction scenario with  $20 \times 5 \text{ cm}^2$  beam size configuration for 50% melted material removed.

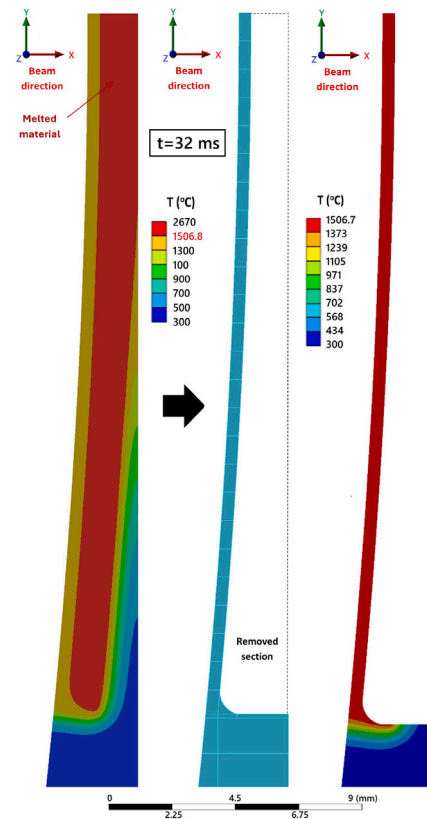


Fig. 12. Reduced model for the 23 mm Li thickness reduction scenario with  $20 \times 5 \text{ cm}^2$  beam size configuration for 75% melted material removed.

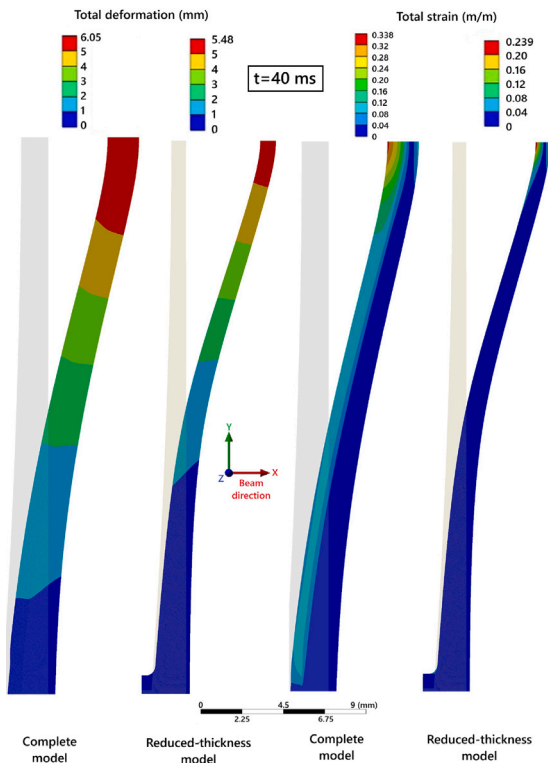


Fig. 13. Structural results for the reduced model for the 13 mm Li thickness reduction scenario with  $20 \times 5 \text{ cm}^2$  beam size configuration and 50% melting.

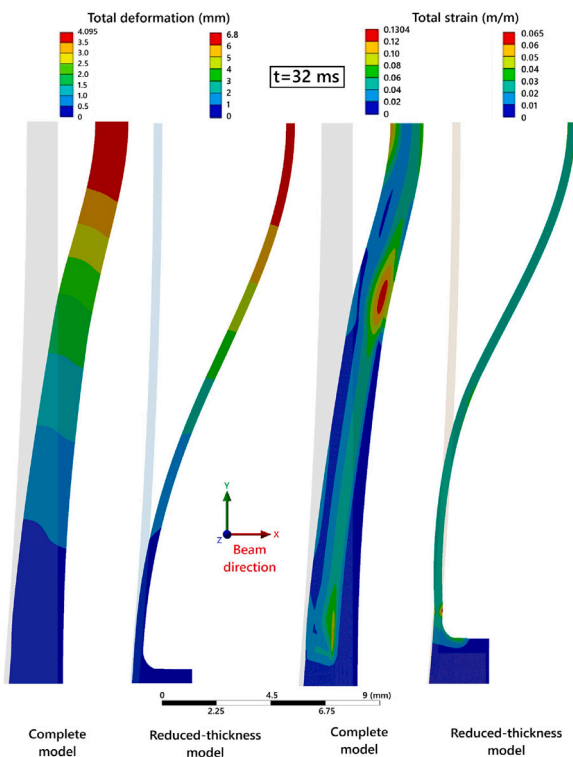


Fig. 14. Structural results for the reduced model for the 23 mm Li thickness reduction scenario with  $20 \times 5 \text{ cm}^2$  beam size configuration and 75% melting.

reductions. For the  $20 \times 5 \text{ cm}^2$  mode, this reduction is above 10 mm, while for the  $10 \times 5 \text{ cm}^2$  mode, it is above 14 mm.

Structural simulations tried to determine timings for reaching the mechanical failure criteria, established at a 30% of strain over a sufficient width on the BP central axis, as the progressive loss of consistency dominates over internal loads. The proposed models foresee that the increasing temperature and subsequent loss of material consistency will lead to the mechanical failure of the solid part of the BP material. This lends support to the assessment that melting 75% of the BP material will induce failure, as there is a positive correlation between increased material removal due to melting and increased total deformation.

In conclusion, simulations suggest that thermal failure criteria is the most appropriate, as the temperatures involved in the range of tens of milliseconds are sufficiently high to provoke the loss of mechanical properties fast enough before reaching intense stresses inside the material. This failure criteria is achieved in a range from 33 to 192 ms and from 17 to 150 ms for the  $20 \times 5$  and  $10 \times 5 \text{ cm}^2$  beam size configurations, respectively. These ranges are important for defining the maximum times for triggering the beam shutdown if instabilities are detected in the lithium curtain during operation.

After failure occurs, the entry of helium from the TC into the beam vacuum would favor the mobilization of activated material upstream through the accelerator beam tube. The amount of this mobilizable airborne material will account for both liquid and gaseous material at the time of failure, along with the addition of a safety margin to consider that the beam may continue to irradiate for some time thereafter. Conservatively, 50 ms have been considered until the passive beam shutdown occurs due to the loss of vacuum in the cryomodules upstream in the beam line, in view of the preliminary results of the MuVacAS (Multipurpose Vacuum Accident Scenarios) experimental campaign concerning propagation velocity after a sudden loss of vacuum and gas entrance in the beam line.

In order to continue in the future analysis with the assessment of the consequences resulting from the entire accident sequence derived from the BP failure, the next evaluations for this purpose will be translated into an amount of activated material that could reach a worker inside the facility or a member of the public outside. To this end, it will be necessary to estimate the amount of respirable airborne mobilizable material that could potentially escape from the different containment structures in the path to representative locations for workers (outside the beam tube) and the public (outside the boundaries of the IFMIF-DONES complex). These assumptions shall take into account the effect of atmospheric dispersion through the determination of local weather conditions, if necessary.

In addition, the results of this future analysis will be essential in defining the requirements for various safety devices that may be installed across the potential path of the activated material, such as the fast isolation valves in the beam tube that will act as confinement barriers by closing in case of detection of increasing pressure in the beam tube.

**CRedit authorship contribution statement**

**M.A. Vázquez-Barroso:** Writing – original draft, Visualization, Software, Methodology, Formal analysis, Data curation, Conceptualization. **C. Torregrosa-Martín:** Writing – review & editing, Supervision, Methodology, Conceptualization. **J. Maestre:** Writing – review & editing, Validation, Supervision, Software, Conceptualization.

**Declaration of Generative AI in Scientific Writing**

During the preparation of this work the authors used ChatGPT and DeepL in order to improve the readability of the work. After using those tools/services, the authors reviewed and edited the content as needed and take full responsibility for the content of the publication.

## Declaration of competing interest

The authors declare that they have no known competing financial interests or personal relationships that could have appeared to influence the work reported in this paper.

## Acknowledgments

This work has been financed by the Consejo de Seguridad Nuclear through the “Subvención de I+D+i SUBV-12/2021 Ref. PR-051-2021”. In addition, it has been carried out within the framework of the EUROfusion Consortium, funded by the European Union via the Euratom Research and Training Programme (Grant Agreement No 101052200 — EUROfusion). Views and opinions expressed are however those of the authors only and do not necessarily reflect those of the European Union or the European Commission. Neither the European Union nor the European Commission can be held responsible for them.

## Data availability

The data that has been used is confidential.

## References

- J. Leis, et al., Report on the international fusion irradiation facility, in: IEA Workshop San Diego, USA, Febr, 1989, pp. 14–17.
- Á. Ibarra, F. Arbeiter, D. Bernardi, M. Cappelli, A. García, R. Heidinger, W. Królas, U. Fischer, F. Martín-Fuertes, G. Micciché, et al., The IFMIF-DONES project: preliminary engineering design, Nucl. Fusion 58 (10) (2018) 105002, <http://dx.doi.org/10.1088/1741-4326/aad91f>.
- D. Stork, P. Agostini, J. Boutard, D. Buckthorpe, E. Diegele, S. Dudarev, C. English, G. Federici, M. Gilbert, S. González, et al., Materials R&D for a timely DEMO: Key findings and recommendations of the EU roadmap materials assessment group, Fusion Eng. Des. 89 (7) (2014) 1586–1594, <http://dx.doi.org/10.1016/j.fusengdes.2013.11.007>.
- Á. Ibarra, R. Heidinger, P. Barabaschi, F. Mota, A. Mosnier, P. Cara, F. Nitti, A stepped approach from IFMIF/EVEDA toward IFMIF, Fusion Sci. Technol. 66 (1) (2014) 252–259, <http://dx.doi.org/10.13182/FST13-778>.
- A. Donné, W. Morris, X. Litaudon, C. Hidalgo, D. McDonald, H. Zohm, E. Diegele, A. Möslang, K. Nordlund, G. Federici, European research roadmap to the realization of fusion energy eurofusion consortium, 2018, URL <http://hdl.handle.net/10138/293624>.
- Ministerio de Industria y Energía, Real decreto 1836/1999, de 3 de diciembre, por el que se aprueba el reglamento sobre instalaciones nucleares y radiactivas, 1999, pp. 46463–46482, URL <https://www.boe.es/eli/es/rd/1999/12/03/1836>.
- Ministerio de Industria, Turismo y Comercio, Real decreto 35/2008, de 18 de enero, por el que se modifica el reglamento sobre instalaciones nucleares y radiactivas, aprobado por real decreto 1836/1999, de 3 de diciembre, 2008, pp. 8858–8871, URL <https://www.boe.es/eli/es/rd/2008/01/18/35>.
- Consejo de Seguridad Nuclear, Instrucción IS-26, de 16 de junio de 2010, del consejo de seguridad nuclear, sobre requisitos básicos de seguridad nuclear aplicables a las instalaciones nucleares, 2010, pp. 60215–60229, URL <https://www.boe.es/eli/es/ins/2010/06/16/is26>.
- C. Torregrosa, et al., Safety engineering approach and licensing strategy of IFMIF-DONES, Submitt. Nucl. Fusion (2024).
- F. Martín-Fuertes, M. García, P. Fernández, A. Cortés, G. D’Ovidio, E. Fernández, T. Pinna, M. Porfiri, U. Fischer, F. Ogando, et al., Integration of safety in IFMIF-DONES design, Safety 5 (4) (2019) 74, <http://dx.doi.org/10.3390/safety5040074>.
- I. Podadera, P. Cara, I. Álvarez-Castro, M. Anguiano, F. Arbeiter, S. Beceril, D. Bernardi, J. Castellanos, N. Chauvin, T. Dézsi, J. Díaz, A. Díez, M. García, S. Gordeev, R. Hernández, M. Luque, L. Macià, J. Maestre, F. Mota, F. Nitti, C. Oliver, J. Park, D. Poljak, C. Prieto, Y. Qiu, D. Sánchez-Herranz, M. Sanmartí, A. Serikov, M. Serrano, T. Tadic, M. Ternerro, C. Torregrosa-Martín, Á. Ibarra, Update of the 5 MW beam-on-target requirements for improvement of the materials irradiation performance at IFMIF-DONES, Nucl. Mater. Energy 40 (2024) 101691, <http://dx.doi.org/10.1016/j.nme.2024.101691>.
- Y. Qiu, F. Arbeiter, D. Bernardi, M. Frisoni, S. Gordeev, R. Hernández, A. Serikov, Potential use of IFMIF-DONES target back-plate for material specimens, J. Nucl. Eng. 3 (4) (2022) 385–397, <http://dx.doi.org/10.3390/jne3040025>.
- A. Dallochio, Study of Thermo-Mechanical Effects Induced in Solids by High Energy Particle Beams: Analytical and Numerical Methods (Ph.D. thesis), Turin Polytechnic, 2008, URL <https://cds.cern.ch/record/1314219>.
- J. Maestre, C. Bahamonde, I. Lamas García, K. Kershaw, N. Biancacci, J. Busom, M. Frankl, A. Lechner, A. Kurtulus, S. Makimura, N. Nakazato, A. Pérez, A. Perillo-Marcone, B. Salvant, R. Seidenbinder, L. Teofili, M. Calviani, High intensity proton beam impact at 440 GeV/c on Mo and Cu coated CFC/graphite and SiC/SiC absorbers for beam intercepting devices, JINST 17 (2022) P01019, <http://dx.doi.org/10.1088/1748-0221/17/01/p01019>.
- C. Torregrosa, Comprehensive Study for an Optimized Redesign of the CERN’s Antiproton Decelerator Target (Ph.D. thesis), Polytechnic University of Valencia, 2018, URL <https://cds.cern.ch/record/2314375>.
- M. Scapin, L. Peroni, A. Dallochio, Thermo-mechanical modelling of high energy particle beam impacts, in: Numerical Modeling of Materials under Extreme Conditions, Springer Berlin Heidelberg, ISBN: 978-3-642-54258-9, 2014, pp. 87–106, [http://dx.doi.org/10.1007/978-3-642-54258-9\\_4](http://dx.doi.org/10.1007/978-3-642-54258-9_4).
- J. Ziegler, M. Ziegler, J. Biersack, SRIM – The stopping and range of ions in matter (2010), Nucl. Instrum. Methods Phys. Res. Sect. B: Beam Interact. Mater. Atoms 268 (11) (2010) 1818–1823, <http://dx.doi.org/10.1016/j.nimb.2010.02.091>, 19th International Conference on Ion Beam Analysis.
- Y. Nie, C. Fichera, L. Mettler, F. Carra, R. Schmidt, N. Tahir, A. Bertarelli, D. Wollmann, Simulation of hydrodynamic tunneling induced by high-energy proton beam in copper by coupling computer codes, Phys. Rev. Accel. Beams 22 (2019) 014501, <http://dx.doi.org/10.1103/PhysRevAccelBeams.22.014501>.
- F. Tavassoli, Fusion demo interim structural design criteria (DISDC)/appendix a material design limit data/A3. S18E eurofer steel, 2004, CEA, EFDA\_TASK\_TW4-TTMS- 005- D01. URL <https://rb.gy/ra3864>.
- K. Mergia, N. Boukos, Structural, thermal, electrical and magnetic properties of Eurofer97 steel, J. Nucl. Mater. 373 (2008) 1–8, <http://dx.doi.org/10.1016/j.jnucmat.2007.03.267>.
- D. Brimbal, L. Beck, O. Troeber, E. Gaganidze, P. Trocellier, J. Aktaa, R. Lindau, Microstructural characterization of eurofer-97 and eurofer-ODS steels before and after multi-beam ion irradiations at JANNUS saclay facility, J. Nucl. Mater. (ISSN: 0022-3115) 465 (2015) 236–244, <http://dx.doi.org/10.1016/j.jnucmat.2015.05.045>.
- G. Aiello, J. Aktaa, F. Cismondi, G. Rampal, J. Salavy, F. Tavassoli, Assessment of design limits and criteria requirements for Eurofer structures in TBM components, J. Nucl. Mater. (ISSN: 0022-3115) 414 (1) (2011) 53–68, <http://dx.doi.org/10.1016/j.jnucmat.2011.05.005>.
- C. Kim, Thermophysical properties of stainless steels, 1975, <http://dx.doi.org/10.2172/4152287>, U.S. Office of Scientific and Technical Information.
- K. Yamaguchi, S. Ueda, High temperature enthalpy measurement of SUS340 stainless steel, High Temp. Mater. Process. 30 (6) (2011) 569–572, <http://dx.doi.org/10.1515/htmp.2011.115>.
- M. Adak, C. Soares, Effects of different restraints on the weld-induced residual deformations and stresses in a steel plate, Int. J. Adv. Manuf. Technol. 71 (2014) 699–710, <http://dx.doi.org/10.1007/s00170-013-5521-9>.
- P. Arasaratnam, K. Sivakumaran, M. Tait, True stress-true strain models for structural steel elements, Int. Sch. Res. Not. 2011 (2011) <http://dx.doi.org/10.5402/2011/656401>.
- American Iron and Steel Institute and American Iron and Steel Institute. Committee of Structural Steel Producers, High-Temperature Characteristics of Stainless Steels, in: Designers’ Handbook Series, Committee of Stainless Steel Producers, American Iron and Steel Institute, 1979, URL <https://books.google.es/books?id=v-j0mQEACAAJ>.
- E. Gaganidze, H. Schneider, B. Dafferner, J. Aktaa, High-dose neutron irradiation embrittlement of RAFM steels, J. Nucl. Mater. (ISSN: 0022-3115) 355 (1) (2006) 83–88, <http://dx.doi.org/10.1016/j.jnucmat.2006.04.014>.
- M. Graham, J. King, T. Pavlov, C. Adkins, S. Middlemas, D. Guillen, Impact of neutron irradiation on the thermophysical properties of additively manufactured stainless steel and inconel, J. Nucl. Mater. (ISSN: 0022-3115) 549 (2021) 152861, <http://dx.doi.org/10.1016/j.jnucmat.2021.152861>.
- M. Meyers, Dynamic Behavior of Materials, John Wiley & Sons, Ltd, ISBN: 9780470172278, 1994, <http://dx.doi.org/10.1002/9780470172278>.
- Y. Guo, M. Zhou, X. Sun, L. Qian, L. Li, Y. Xie, Z. Liu, D. Wu, L. Yang, T. Wu, D. Zhao, J. Wang, H. Zhao, Effects of temperature and strain rate on the fracture behaviors of an Al–Zn–Mg–Cu alloy, Materials (ISSN: 1996-1944) 11 (7) (2018) <http://dx.doi.org/10.3390/ma11071233>.
- I. Gilath, S. Eliezer, M. Dariel, L. Kornblit, Total elongation at fracture at ultra-high strain rates, Mater. Sci. Lett. 7 (1988) 915–917, <http://dx.doi.org/10.1007/BF00720728>.